Magnetic Resonance Materials in Physics, Biology and Medicine
https://doi.org/10.1007/s10334-026-01368-1

RESEARCH ARTICLE

Reducing scan time burden for neonatal MRI of pulmonary structure using FLORET UTE

Andrew D. Hahn[1] · Matt M. Willmering[2,3,4,5] · Nara S. Higano[2,3,4] · Conner J. Wharff[1] · Robert J. Fleck[5,6] · Robert P. Guillerman[6,7] · Jason S. Woods[2,3,4,5,8] · Sean B. Fain[1,9,10,11,12]

Received: 17 November 2025 / Revised: 24 April 2026 / Accepted: 29 April 2026

Abstract

Objective Pulmonary MRI in neonates can be performed with quality comparable to radial 3D ultrashort echo time (UTE) MRI in significantly less time using a FLORET trajectory.

Materials and methods Eighteen NICU patients with severe bronchopulmonary dysplasia (BPD), age 40.9 ± 3.0 weeks at time of imaging, underwent MRI using Radial and FLORET UTE at 1.5 T. Pulmonary signal-to-noise ratio (SNR), lung density, and radiologist scoring of motion artifacts and image quality were compared across sequence types.

Results FLORET UTE reduced scan time by ~ 75% (4:40 vs. 16:41 min.) while incurring only ~ 10–30% SNR reduction vs. radial (radial vs. 1-hub FLORET: 9.8 ± 2.8 vs. 9.0 ± 2.6, radial vs. 3-hub FLORET: 9.2 ± 3.0 vs. 7.7 ± 2.3), $P < 0.05$. Normalized lung density measurements were elevated in FLORET (radial vs. 1-hub FLORET: 0.42 ± 0.13 vs. 0.49 ± 0.14, radial vs. 3-hub FLORET: 0.49 ± 0.13 vs. 0.51 ± 0.13), $P < 0.05$. Accounting for scan time differences, normalized radial SNR was 19% and 16% lower than 1-hub and 3-hub FLORET, respectively ($P < 0.05$). No significant differences in radiologist scores were found.

Conclusion FLORET UTE images are of quality comparable to radial UTE at 75% of the total scan time, the current state of the art, and have a much greater time-SNR efficiency with enormous benefit in the neonatal population.

Keywords Neonatal MRI · Ultrashort echo time · FLORET · Lung

Introduction

Radial 3D ultrashort echo time (UTE) MRI [1] has been developed over the past several years as a tool for clinical evaluation of lung disease in infants within the neonatal intensive care unit (NICU) [2–9]. A number of studies have demonstrated its utility for detecting clinically relevant pulmonary abnormalities in patients with bronchopulmonary dysplasia (BPD) [4, 6, 10, 11] and congenital diaphragmatic hernia (CDH) [3]. Imaging of the central airway in NICU

✉ Sean B. Fain
sean-fain@uiowa.edu

1 Department of Radiology, University of Iowa, Iowa City, IA, USA

2 Center for Pulmonary Imaging Research, Division of Pulmonary Medicine, Cincinnati Children's Hospital Medical Center, Cincinnati, OH, USA

3 Bronchopulmonary Dysplasia Center, Cincinnati Children's Hospital, Cincinnati, OH, USA

4 Imaging Research Center, Department of Radiology, Cincinnati Children's Hospital Medical Center, Cincinnati, OH, USA

5 Department of Pediatrics, University of Cincinnati, Cincinnati, OH, USA

6 Department of Radiology, Cincinnati Children's Hospital, Cincinnati, OH, USA

7 Department of Radiology, University of Cincinnati, Cincinnati, OH, USA

8 Department of Physics, University of Cincinnati, Cincinnati, OH, USA

9 Advanced Pulmonary Physiomic Imaging Laboratory, University of Iowa, Iowa City, IA, USA

10 Department of Biomedical Engineering, University of Iowa, Iowa City, IA, USA

11 Department of Electrical and Computer Engineering, University of Iowa, Iowa City, IA, USA

12 Department of Health and Human Physiology, University of Iowa, Iowa City, IA, USA

Published online: 14 May 2026

patients has also been a significant focus recently using this technique [7–9, 12–15]. Moreover, parametric mapping of R_2* has been investigated and may be sensitive to pulmonary disease processes in BPD and CDH, pending further studies with acquisitions at expanded echo times [16, 17]. However, reducing scan time is important in this young and delicate patient population, which is often prone to low and/or unpredictable subject compliance, especially if the technique is used in less stable patients.

Two of the most important characteristics of the radial UTE scan are its inherent robustness to motion due to the pseudorandomized projection view order and self-navigation for retrospective respiratory gating [18], allowing it to be performed during quiet tidal breathing. With neonatal patients' small anatomies (e.g., total lung capacity of 180–250 ml) and the low sampling efficiency of 3D radial trajectories, long scan times are necessary to achieve high isotropic 3D resolution (~ $1mm^3$) (e.g., ~ 15 min in a neonate vs. ~ 5 min in an adult). Thus, despite the proven track record of radial UTE, this can be a difficult component of imaging exams in NICU patients, given that limiting the duration of individual scans and the overall exam is a practical consideration that is important for patient safety and motion mitigation. This is particularly the case for parametric mapping scans, with scan times as long as 20 min, making routine use impractical [16].

In recent years, more efficient strategies for sampling k-space with UTE MRI properties have been proposed [19, 20]. These "center-out" acquisition schemes utilize spiral or otherwise curved trajectories in k-space that are more uniformly sampled and require fewer excitation shots to achieve full Nyquist sampling. Indeed, work has already been published that applies these techniques specifically for lung imaging [21, 22], indicating that they are viable, and crucially more efficient [23], alternatives to radial UTE.

The main goal of this work is to explore the application of a more efficient 3D UTE sampling strategy to neonatal lung imaging—specifically FLORET [19] UTE, in order to achieve desirably shorter scan durations compared to radial acquisitions. Additionally, the transverse relaxation rate, T_2*, in pulmonary tissue in neonates is longer than observed in adults (~ 3 ms vs. 2.1 ms at 1.5 T) [16], allowing for longer readouts, optimally on the order of T_2* [21], further improving the sampling efficiency.

Overall, we hypothesize that UTE MRI in neonates can be performed with comparable image quality in significantly less time using a FLORET trajectory as opposed to an optimized radial UTE with variable density sampling. Furthermore, we expect similar motion robustness and retrospective respiratory gating capabilities using both techniques. Ghosting/aliasing artifacts should be minimal when sampling at or above the Nyquist limit, and otherwise incoherent leading to similar degradation in image quality in both trajectories. To isolate deterministic vs physiologic sources of noise, we perform imaging experiments in a phantom to verify relative performance expectations of radial and FLORET UTE, and then test our main hypothesis in a cohort of NICU patients with BPD.

Materials and methods

Theory

Signal to noise

The SNR sampling efficiency [23] of an MRI acquisition, W_{eff}, can be described in terms of sampling density, w_m, at each sampled point m, where M is the total number of samples, as:

$$W_{\text{eff}} = \frac{\sum_{m=1}^{M} w_m}{\sqrt{M \sum_{m=1}^{M} w_m^2}}. \quad (1)$$

In the case of uniform sampling (i.e., Cartesian), the SNR efficiency is equal to unity. However, non-Cartesian sampling patterns necessarily oversample parts of k-space, which results in inefficiencies. Thus, the sampling efficiency is a tool for computing how much each sample in an acquisition contributes to SNR relative to a Cartesian acquisition, all else being equal. Given the same number of acquired samples and otherwise identical scan parameters (e.g., bandwidth, TR, TE, flip angle, resolution, etc.), the relative SNR of two sequences should be given by Eq. 1.

Sampling

To compare sampling efficiency between radial and FLORET trajectories, we define a figure of merit that accounts for scan time and coverage. Of course, the time required to *fully sample* k-space depends on the sequence trajectory used. For example, the number of views, N_v, required using a 3D radial trajectory scales with the field of view and resolution but is independent of the readout time per view. On the other hand, FLORET trajectories typically require far fewer views, particularly for longer readout times [23], because samples within a given view are not confined purely to radial spokes. Therefore, using radial sampling, each additional readout point simply adds additional time proportional to the required number of views,N_v. In other words, the total scan time increases by $N_v \times (TR + N_{x,\text{add}} \times t_s)$, where $N_{x,\text{add}}$ is the number of additional readout samples, t_s is the sampling rate, and TR is the original repetition time. Thus, the relative scan time increase is $\frac{(TR+N_{x,\text{add}} \times t_s)}{TR}$. Note that nominal image resolution can remain the same with the added

samples by reducing the readout gradient amplitude accordingly (keeping t_s the same). On the other hand, FLORET requires fewer views as readout time (number of readout samples) increases, leading to a relative change in scan time by an amount given by $\frac{N_{v,\text{add}} \times (TR + N_{x,\text{add}} \times t_s)}{N_v \times TR}$, where $N_{v,\text{add}}$ is the number of required views when acquiring longer readouts and $N_{v,\text{add}} \leq N_v$.

Tradeoffs

From Eq. 1, relative SNR scales with the square root of the relative number of samples acquired. SNR of radial trajectories can, therefore, be increased significantly by using a variable density readout [1], which both increases the number of readout samples per view for a given resolution and improves W_{eff} such that SNR can be made roughly equivalent to its FLORET counterpart. However, scan time is another issue because FLORET can acquire fewer total samples (in less time) to achieve equivalent sampling, with the relatively benign tradeoff that the SNR is reduced only by the square root dependence on the relative number of samples.

However, another variable that governs the density of sampling when using the FLORET trajectory is the number of hubs along the 3 orthogonal orientations of k-space. We note that the tradeoff between a 1-hub and 3-hubs FLORET implementation is also described by sampling efficiency. Acquiring multiple hubs allows smaller values of α_0 (the maximum cone angle), which improves intra-trajectory sample spacing. However, this comes at the cost of orthogonal oversampling, i.e., hub overlap that does not occur in 1-hub designs [19]. However, it may be that the oversampling inherent in the 3-hubs implementation is beneficial when retrospectively undersampling for respiratory gating. The value of α_0 (45°) for 3-hub FLORET was chosen here as a reasonable tradeoff between improved $\text{SNR}_{\text{efficiency}}$ and orthogonal oversampling.

Clinically used scan parameters for radial UTE result in a total scan time of 16:40 [2, 5], achieving nearly fully sampled k-space data (undersampling factor of ~ 0.97). Based on the expected improvement in sampling efficiency afforded by FLORET, we can achieve equivalent undersampling using a 3.5 ms readout (compared to 2.0 ms readout using radial UTE), approximately equal to neonatal lung T_2* at 1.5 T [16], with a reduction of scan time to 2:02 (88% reduction) and 2:48 (83% reduction) using 1-hub and 3-hubs designs, respectively. However, these would result in a reduction in expected SNR relative to the radial equivalent by ~ 42% and ~ 52%, respectively, which was judged to be too high a tradeoff given the low proton density in the lungs [2]. Our strategy was to empirically balance this tradeoff to retain the same sampling efficiency but mitigate the SNR loss by oversampling the FLORET acquisition by approximately a factor of 2 (relative to full Nyquist sampling), which will also help with retrospective respiratory gating. This approach maintains a substantial ~ 75% reduction in scan time but with a less severe reduction in SNR of 18% and 32% relative to the radial equivalent for a 1-hub and 3-hub implementation, respectively.

Phantom experiments

Imaging experiments in a phantom were performed to validate the theoretically expected relative SNR efficiency performance of radial and FLORET acquisitions in the absence of physiologic and disease-based variations. The phantom consisted of five glass vials filled with mixtures of water and deuterium dioxide (D_2O, heavy water) to produce a range of proton densities (10%, 30%, 50% 70% and 90% water). Additionally, $MnCl_2$ was added to reduce the T_2* to a value approximately equal to that expected in the lung of neonates (5 mM concentration, T_2* ≈ 2.7 ms). An image of the phantom is shown in Fig. 1, and a full description of the phantom has additionally been previously published [16]. A phantom with high-resolution features was also used to investigate differences in real image resolution between radial and FLORET trajectories. These experiments are described in the Supplemental Information.

Image acquisition

Imaging of the phantom was performed on a 3 T MRI scanner (Signa Premier, General Electric, Waukesha, WI) using a quadrature head coil. All sequences tested had the following common parameters: FOV = 320 mm, matrix = 320 × 320 × 320, TE = 90 µs, BW = 250 kHz, Flip Angle = 6°. Sequence-specific parameters were as follows: (1) radial UTE (TR = 3.2 ms, # of radial views varied from 12,500–50,000, samples per view = 640), (2) 1-hub FLORET (α_0 = 90, TR = 5.8 ms, # of spiral views varied from 7500–30,000, samples per view = 1500), (3) 3-hub FLORET (α_0 = 37, TR = 5.8 ms, # of spiral views = 7500–30,000, samples per view = 1500). Scan parameters are also provided in Table 1. Each acquisition scheme was repeated four times, reducing the number of views (and thus the total scan time) in each by a factor of 2×, 3× and 4× relative to the first scan in each subsequent repetition. This provides both a range of SNR comparisons against theory and includes relative scan time differences on the order of those used in human studies.

Image processing and analysis

Correction for gradient waveform imperfections was performed using a separate calibration scan [24] to compute the actual k-space trajectories. The acquired non-Cartesian k-space data were then resampled onto a Cartesian grid

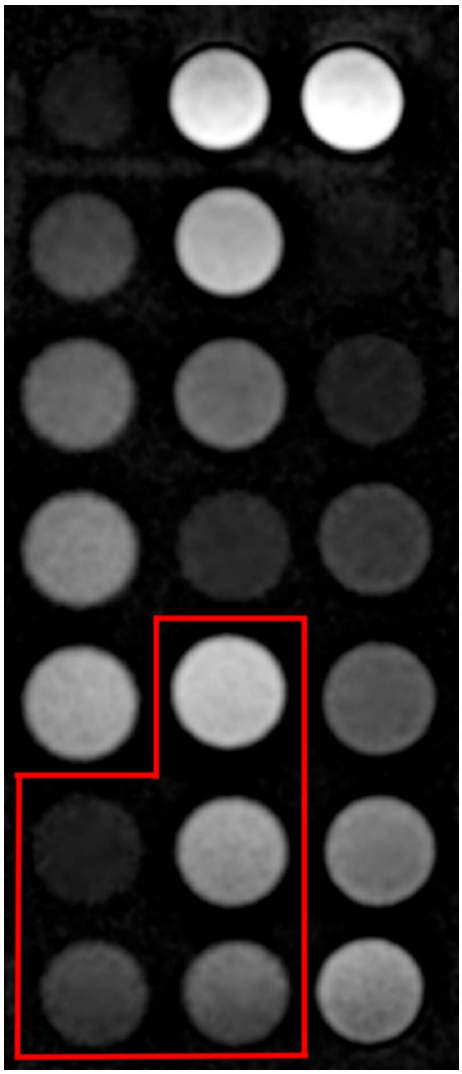

Fig. 1 Single slice from the density/T2* phantom showing a top-down view of the $D_2O/MnCl_2$ doped vials. The vials outlined in red represent those used for these experiments, specifically 5 mM $MnCl_2$ concentration and 10%, 30%, 50%, 70%, and 90% D_2O concentration (from brightest to darkest)

[25] using weights, w_m, calculated iteratively to compensate for the non-uniformly sampled data [26]. Images are generated by inverse Fourier transformation of the uniformly re-gridded k-space data.

The vials in the phantom and a background region of interest (ROI) were each manually segmented using Fiji [27]. The mean signal intensity within each vial was computed and signal-to-noise ratio (SNR) was estimated by dividing by the standard deviation of the signal in the background ROI.

For comparison of the SNR across each sequence, the following normalization was applied:

Table 1 Acquisitions and specific parameters tested for phantom and neonatal patient studies

Scan type	FOV (mm)	Resolution (mm)	TE (ms)	TR (ms)	Flip angle	Views	Readout Pts	Readout Duration (ms)	α_0	Scan time	SNR efficiency	Oversampling factor
3D Radial—phantom	320	1	0.09	3.2	6	12,500–50,000	640	1.3	N/A	0:40–2:40	0.88	0.04–0.16
1-hub FLORET—phantom	320	1	0.09	5.8	6	7500–30,000	1500	3.0	90	0:44–2:54	0.86	0.24–0.96
3-hub FLORET—phantom	320	1	0.09	5.8	6	7500–30,000	1500	3.0	37	0:44–2:54	0.88	0.19–0.78
3D Radial—Human	180	0.7	0.16	5	5	200,000	1012	2.0	N/A	16:41	0.93	0.97
1-hub FLORET—Human	180	0.7	0.16	7	5	40,000	1750	3.5	90	4:40	0.85	2.41
3-hub FLORET—Human	180	0.7	0.16	7	5	45,000	1750	3.5	45	5:13	0.91	1.81

$$\mathrm{SNR}_{\mathrm{norm}} = \mathrm{SNR}/(W_{\mathrm{eff}} \times \sqrt{N_v N_x} \times M_{\perp}) \tag{2}$$

$$M_{\perp} = \sin(\mathrm{FA}) * \frac{(1 - e^{-TR/T_1})}{1 - \cos(\mathrm{FA}) \times e^{-TR/T_1})} \tag{3}$$

to remove known dependencies of the measured SNR on the sampling density, flip angle and T_1 recovery, where N_v and N_x are the number of views and the number of sampled points per view, respectively, and their product is equivalent to the total number of acquired points, M. $M_{\perp}$ is the transverse magnetization weighting associated with the flip angle (FA), TR and T_1, which may vary across sequences. Equivalently, the SNR normalization factor from Eq. 2, $1/(\mathrm{SNR}_{\mathrm{efficiency}} \times \sqrt{N_v N_x} \times M_{\perp})$, can be expressed such that the dependence on total scan time and readout duration is made more explicit (as opposed to the dependence on total number of samples) [28]:

$$\mathrm{SNR}_{\mathrm{norm}} = \frac{\mathrm{SNR}}{\left(W_{\mathrm{eff}} \times \sqrt{\frac{2TA}{T_1 + TA}} \sqrt{T\tau}\right)} \tag{4}$$

$$\mathrm{TA} = \frac{-\mathrm{TR}}{\ln(\cos(FA))} \tag{5}$$

where T is the total scan time and τ is the readout duration. The T_1 in the phantom was estimated to be 2.7 ms at a $MnCl_2$ concentration of 5 mM [29]. Despite its very short T_1, this vial was used to assess performance because of its similarity to the T_2* of the lungs. The experimental T_1 was used to correct for SNR per Eq. 3.

A linear regression was fit to the normalized SNR within each vial for the 1-hub and 3-hub FLORET, and the coefficients (i.e., intercept and slope) were tested for differences from the expected values using a t test, in this case the expected intercept of 0 and a slope of 1.

Human volunteer and patient studies

All studies were conducted with the approval of the Institutional Review Board and parental informed consent (IRB# 2018-0958). MRI was performed on 18 NICU patients with severe BPD (8M/10F, gestational age at birth/MRI = 25.7 ± 2.5/40.9 ± 3.0 weeks, weight at birth/MRI 696 ± 264/3034 ± 612 g), with 3 patients undergoing repeat exams resulting in 21 total datasets. A flow chart of the experimental design is provided in Fig. 2. In all 21 exams, patients were imaged using a variable density readout radial UTE sequence [1]. In 7 of the 21 exams, a 1-hub FLORET UTE sequence was acquired, and in 14 of the 21 exams, a 3-hub FLORET UTE sequence was acquired.

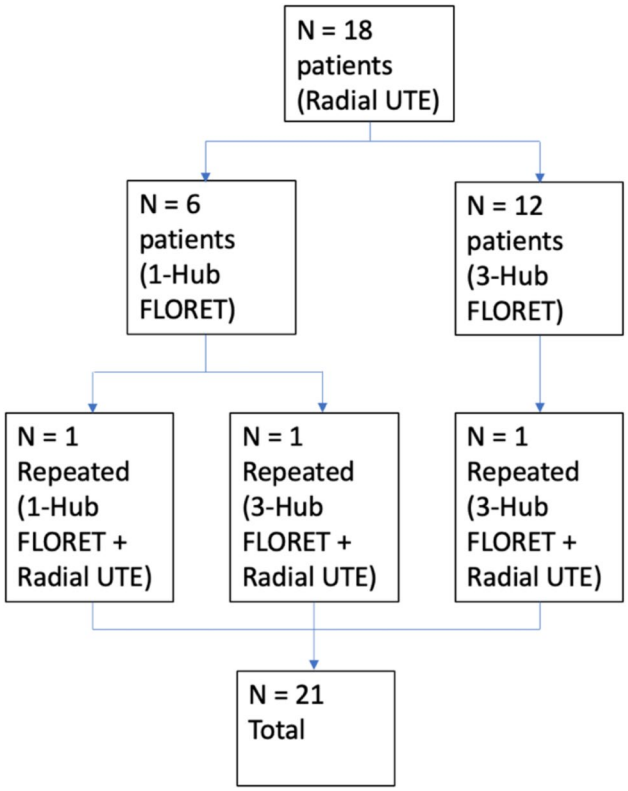

Fig. 2 Flow chart of study population experimental design

Image acquisition

Imaging in the NICU was performed using a 1.5 T scanner designed for neonatal imaging with a quadrature body coil [30] (N = 19) or a dual-tuned H^1/Xe^{129} body coil (N = 2) [31]. Infants were prepared for scanning using the "feed and swaddle" method [32] and were imaged without administration of intravenous contrast agents. Patients were not sedated or on respiratory support unless clinically indicated. Heart rates and SpO_2 levels were monitored throughout the exam.

In all 21 exams, patients were imaged using a variable density readout radial UTE sequence [1] with the following parameters: scan time = 16:41 min., FOV = 180 mm, matrix = 256 × 256 × 256, TE = 160 µs, BW = 250 kHz, Flip angle = 5°, TR = 5.0 ms, # of radial views = 200,000, samples per view = 1012. Patients were additionally imaged with one of two different FLORET sequences during the same exam: (1) 1-hub FLORET (N = 7, scan time = 4:40, α_0 = 90, FOV = 180 mm, matrix = 256 × 256 × 256, TE = 160 µs, BW = 250 kHz, flip angle = 5°, TR = 7.0 ms, # of spiral views = 40,000, samples per view = 1750), or (2) 3-hub FLORET (N = 14, scan time = 5:13, α_0 = 45, FOV = 180 mm, matrix = 256 × 256 × 256, TE = 160 µs, BW = 250 kHz, flip angle = 5°, TR = 7.0 ms, # of spiral views = 45,000, samples per view = 1750). Imaging parameters for all scans are also

provided in Table 1. Assignment of subjects to either 1-hub or 3-hub FLORET was based on time of the scan; the initial set of subjects was imaged with 1-hub, following a full transition of the protocol to 3-hubs approximately 1 month into the period of the study.

Image processing and analysis

Respiratory gating using the "hard gating" method that exploits the repeated sampling of the center of k-space was performed retrospectively, with 50% data acceptance (described previously [18]). Images from both respiratory gated and ungated data were re-gridded and transformed to images, as described for the phantom experiments above.

In each patient, an ROI within the lung with no apparent pathophysiology was manually identified and segmented using Fiji [27]. Additionally, a region of adjacent muscle tissue was similarly manually segmented. Again, a background ROI was segmented for noise estimation. Mean signal intensities within the lung and muscle tissue ROIs, and signal standard deviation from the background were calculated in each reconstructed dataset (radial and FLORET, gated and ungated) to estimate SNR in both muscle and lung. Normalized lung tissue density (TD) was estimated by dividing the lung signal by the adjacent muscle signal [5]. Finally, normalized SNR was estimated for each measurement according to Eq. 1 for comparison across sequences within each patient. In human data, the T_1 in both muscle and lung tissue was assumed to be 1.2 s [33].

Paired *t* tests were used to test for differences in SNR in both muscle and lung, as well as normalized tissue densities, under different acquisition and/or gating schemes. A linear regression was fit to the normalized SNR within each ROI for 1-hub and 3-hub FLORET acquisitions, and the coefficients were compared to the expected values (intercept of 0, slope of 1) using a *t* test.

All 42 image datasets (21 FLORET + 21 radial) were anonymized and scored by two expert radiologists (RJF and RPG) on a Likert scale for apparent motion artifacts (1 non-apparent, 5 severe), diagnostic quality (1 non-diagnostic, 5 excellent), degree of pulmonary pathology (1 none, 5 severe), and last visible airway generation. Scores from both readers were averaged for statistical analysis. Differences in overall medians between radial and FLORET image scores were tested using Wilcoxon rank sum tests, and pairwise differences between radial and FLORET within subjects were tested using Wilcoxon signed rank tests.

Results

Plots of the normalized SNR (Eq. 2) in a phantom are provided in Fig. 3a. Each plotted point represents a D_2O percentage and common FLORET and UTE undersampling factor. These results indicate that the radial and FLORET UTE sequences, each produce the expected SNR after normalization for sampling and physical parameters. This is further supported by the linear regression coefficients for both the 1-hub and 3-hub FLORET vs. the radial UTE normalized for

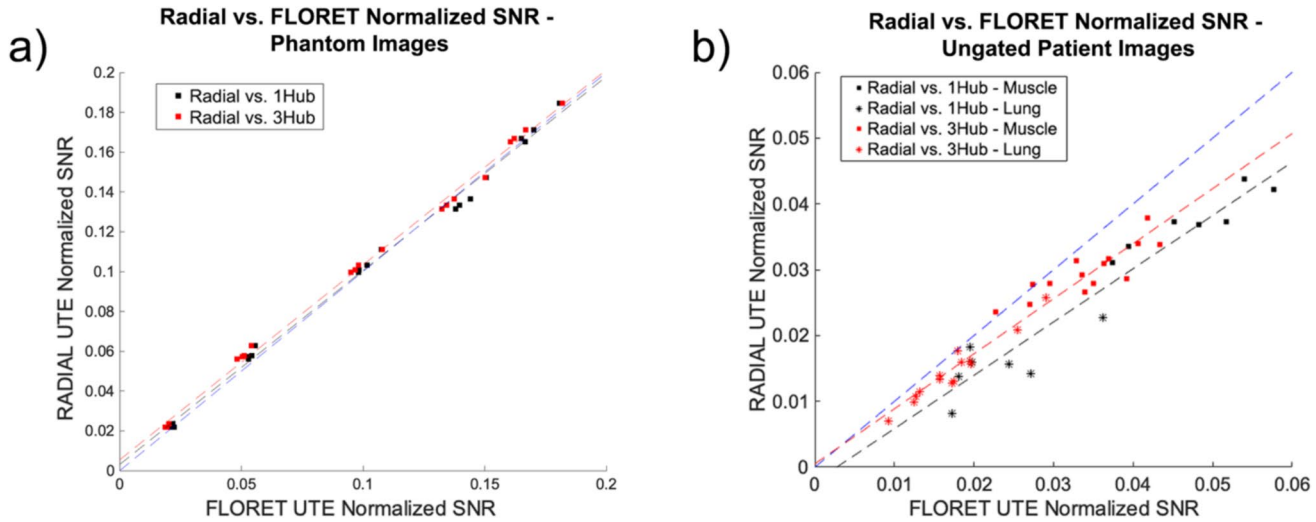

Fig. 3 Scatter plots of the normalized SNR (Eq. 2) in the FLORET vs. radial acquisitions in the density and T_2* phantom (**a**) and in ungated patient images (**b**). The black and red dashed lines depict the linear regression line fit to the data in the radial vs. 1-hub and radial vs. 3-hub data, respectively. The blue dashed line shows the expected trend; normalized SNR should be equivalent across trajectories. Phantom data (**a**) express the expected trend ($R^2_{1\text{-hub}} = 0.97$, $R^2_{3\text{-hub}} = 0.98$); however, human data do not. Human data regression lines ($SNR_{UTE} = -.002 + 0.81 \times SNR_{FLORET,\ 1\text{-hub}}$, $SNR_{UTE} = -0.0005 + 0.84 \times SNR_{FLORET,\ 3\text{-hub}}$) indicate that FLORET measurements are consistently higher than expected relative to their radial UTE counterparts (slope < 1)

SNR; the intercept and slope of these lines are not different than 0 and 1, respectively. Additionally, the relative densities measured in the phantom vials were not significantly different between the same sequences.

Image quality comparisons between the FLORET and radial acquisitions in neonatal subjects (Fig. 4) show similar visualization of pulmonary structural pathology, both showing good contrast between regions of high and low tissue density within the lung. Qualitatively, the SNR is higher in the radial UTE compared to both 1-hub (Fig. 4, top) and 3-hub (Fig. 4, bottom) FLORET acquisitions. Interestingly, the average density of lung parenchyma appears notably

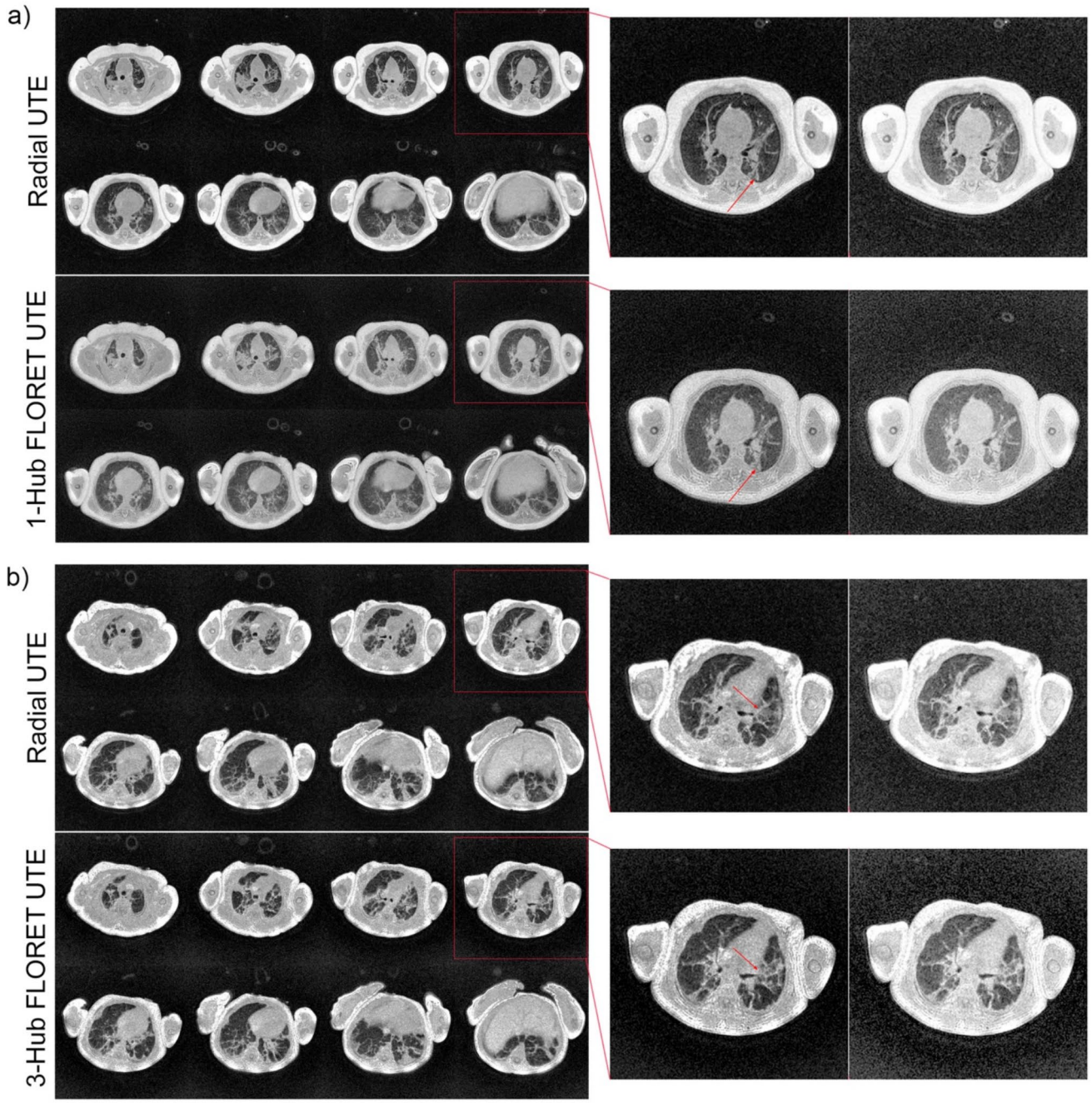

Fig. 4 Axial slices from both radial and FLORET UTE in representative subjects scanned with **a** 1-hub FLORET and **b** 3-hub FLORET. Voxel size is 0.7 mm isotropic with FOV of 180 mm in all cases. In both subjects, lung abnormalities are similarly apparent in both modalities, indicated by the red arrows. Zoomed images at two different window/level settings are provided to both highlight these structural similarities as well as provide better qualitative view of background noise and SNR. The signal intensity within the lung in the 1-hub FLORET images (**a**) appears noticeably higher than in the corresponding radial UTE images

higher in the 1-hub FLORET compared with the radial UTE (Fig. 4, top), while this is not the case with the 3-hub FLORET acquisition (Fig. 4, bottom). The other notable difference between the FLORET and radial images is the interference pattern at fat/water interfaces present in both the 1-hub and 3-hub FLORET acquisitions not seen in the radial UTE for this patient (Figs. 4 and 5).

The effectiveness of the retrospective respiratory gating is demonstrated in Fig. 5. The respiratory motion, which induces blurring at the diaphragm in the ungated images, is not severe in any of these representative images. However, a reduction of blurring at the diaphragm is still apparent following respiratory gating, and neither FLORET nor radial images show apparent undersampling artifacts beyond reduction in SNR. This indicates that both FLORET sequences can be effectively gated retrospectively with a reduction in motion blurring comparable to radial UTE using proven self-gating methods [18].

Quantitative comparison of SNR between radial and FLORET UTE images shows that radial images have a higher SNR for equivalent gating schemes in both muscle and lung tissue with one exception: lung tissue SNR is not statistically significantly different between 1-hub FLORET and radial UTE in the respiratory gated images. This is expected since the radial UTE data were acquired over a 3×–4× longer time period than FLORET, in line with the expectations presented in the *Theory* section above. To emphasize the relationship between acquisition time and SNR in each case, we computed the SNR/second for both trajectories and gating schemes and report these in Table 2. Note that FLORET SNR/sec is ~ 2.5×–3× higher than radial in all cases. Boxplots of these SNR data are provided in Fig. 6, and a full tabulation of these results can be found in Table 2.

Comparison of normalized lung tissue density (TD) yielded unexpected results. Lung tissue density estimates in both gated and ungated FLORET images ($TD_{ungated} = 0.49 \pm 0.14$, $TD_{gated} = 0.49 \pm 0.11$) were significantly ($P < 0.05$) greater than similar measurements in the radial data ($TD_{ungated} = 0.42 \pm 0.13$, $TD_{gated} = 0.42 \pm 0.13$). Similarly, measured tissue densities in the 3-hub FLORET ($TD_{ungated} = 0.51 \pm 0.13$, $TD_{gated} = 0.52 \pm 0.13$) were also greater than those in corresponding radial images ($TD_{ungated} = 0.49 \pm 0.13$, $TD_{gated} = 0.50 \pm 0.13$), but this difference was less pronounced than for 1-hub FLORET and was only statistically significant in the ungated data ($P < 0.05$). Notably as expected, no statistically significant differences in TD were found between gated and ungated data for the same sequence type within any of the 3 acquisition trajectories. Boxplots of tissue density comparisons are provided in Fig. 7.

Plots of the normalized SNR (Eq. 2) in the lungs for the neonatal data are shown in Fig. 3b. Here, each point represents normalized SNR from radial (x-axis) and FLORET (y-axis) acquisitions within a single subject in either lung or muscle tissue. These indicate that SNR is higher in both

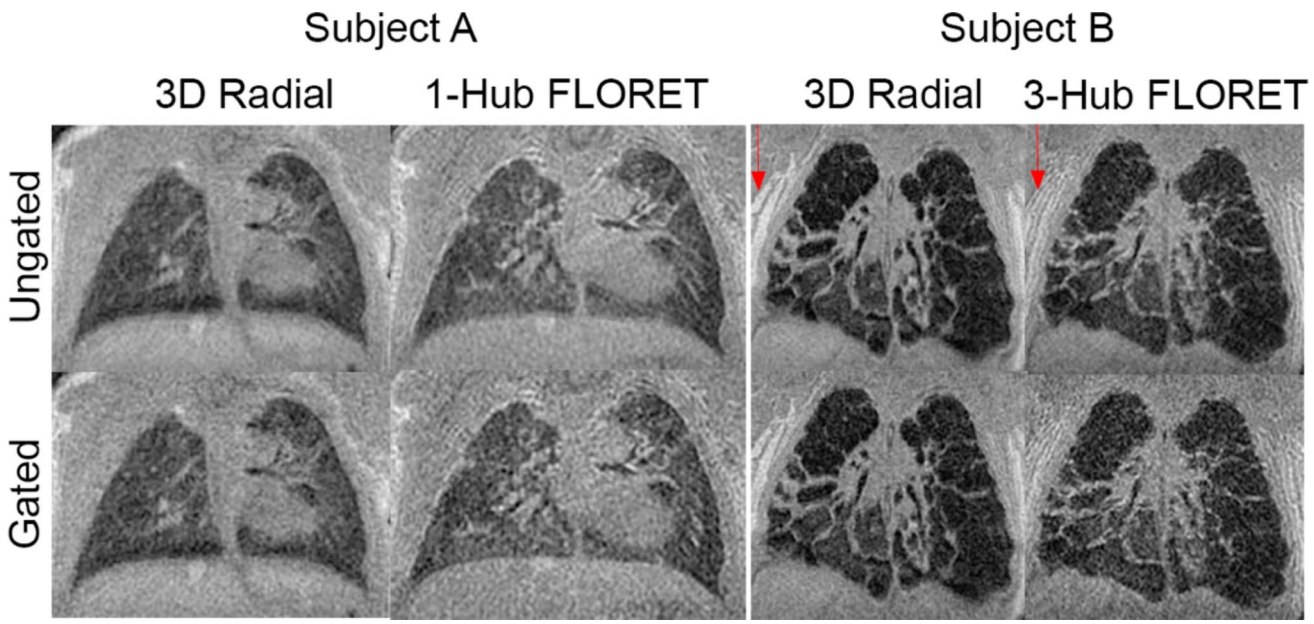

Fig. 5 Coronal views from two NICU patients demonstrating the effect of retrospective respiratory gating in both radial and FLORET UTE. The boundary at the diaphragm is noticeably more defined in the gated images. Overall, image quality is generally comparable between radial and FLORET acquisitions, although SNR in FLORET appears somewhat lower. Also of note is the difference in fat–water interference in the chest wall for radial vs. FLORET images, indicated by the red arrows

Table 2 Experimental results for SNR and SNR/second by tissue type in patient studies for each method tested (SNR is normalized to the SD of outside noise, tissue density is normalized to chest wall muscle)

Scan type	Lung SNR—ungated	Lung SNR/sec—ungated	Lung SNR—gated	Lung SNR/sec—gated	Muscle SNR—ungated	Muscle SNR/sec—ungated	Muscle SNR—gated	Muscle SNR/sec—gated	Tissue Density—ungated	Tissue density—gated
Radial (paired w/ 1-hub FLORET)	9.8 ± 2.8	0.0098 ± 0.0028	6.5 ± 2.0	0.0065 ± 0.0020	23.5 ± 2.8	0.0235 ± 0.0028	15.6 ± 1.4	0.0156 ± 0.0014	0.42 ± .13	0.42 ± .13
1-hub FLORET	9.0 ± 2.6	0.0321 ± 0.0093	6.2 ± 1.5	0.021 ± 0.0054	18.4 ± 2.9	0.0657 ± 0.0104	12.7 ± 1.1	0.0454 ± 0.0039	0.49 ± .14	0.49 ± .11
Radial (paired w/ 3-hub FLORET)	9.2 ± 3.0	0.0092 ± 0.0030	6.9 ± 2.3	0.0069 ± 0.0023	18.7 ± 2.4	0.0187 ± 0.0024	13.6 ± 2.0	0.0136 ± 0.0020	0.49 ± .13	0.50 ± .13
3-hub FLORET	7.7 ± 2.3	0.0246 ± 0.0073	5.7 ± 1.7	0.018 ± 0.0054	15.2 ± 2.7	0.0486 ± 0.0086	10.4 ± 1.8	0.0332 ± 0.0058	0.51 ± .13	0.52 ± .13

1-hub and 3-hub FLORET data relative to radial, and this unexpected normalized SNR difference is even more pronounced in the 1-hub data. This is quantitatively confirmed by the slope of the regression line which is significantly less than 1 in both cases ($\beta_{1,1\text{-hub}} = 0.81$, 95% CI [0.66, 0.96]; $\beta_{1,3\text{-hub}} = 0.84$, 95% CI [0.75, 0.92]). However, the regression line intercept is not significantly offset from 0 in either the 1-hub or 3-hub data ($\beta_{0,1\text{-hub}} = -0.002$, 95% CI [−0.008, 0.003]; $\beta_{0,3\text{-hub}} = -0.0005$, 95% CI [−0.002, 0.003]). While this finding is unexpected, it is consistent with the large differences in normalized tissue density described above.

Radiologic assessment of diagnostic image quality was very similar between radial (2.71 ± 0.83) and FLORET (2.64 ± 0.96). Degree of structural pathology was also very similar between radial (3.26 ± 0.74) and FLORET (3.31 ± 0.62). Also in the same vein, the last visible airway generation for radial (2.19 ± 0.78) and FLORET (2.17 ± 0.76) were nearly identical. None of these results show statistically significant differences. Finally, FLORET had slightly better scores for appearance of motion artifacts (2.67 ± 1.00) than radial (2.95 ± 1.00); however, the difference was, again, not statistically significant ($P = 0.35$ and $P = 0.29$ for population and pairwise differences, respectively) (Table 3).

Discussion

This work demonstrates that a scan time reduction from 16:40 to 4:40 min can be achieved by switching to a FLORET acquisition from a radial UTE acquisition with comparable image quality in NICU patients. Despite this large reduction in scan time, FLORET UTE incurs only a 20—30% penalty in SNR while producing images that depict qualitatively and quantitatively similar pulmonary structural pathology after retrospective respiratory gating during quiet breathing. This scan time reduction can improve the safety and routine accessibility of pulmonary UTE in the NICU and enable more quantitative techniques, such as parametric mapping of T_1 and T_2, that would typically require prohibitively long scan times.

Further improvement in FLORET image quality is achievable. While phantom experiments indicate our implementations of FLORET and radial UTE have the expected relative performance in terms of normalized SNR, we found deviations from this expected performance in vivo. Both 1-hub and 3-hub FLORET trajectories yielded higher than expected SNR in both muscle and lung tissue relative to radial UTE performance. Furthermore, this SNR increase was not proportional across the range of SNR in the 1-hub FLORET images; lung tissue had a disproportionately larger signal increase (compared to muscle tissue) such that the estimate of normalized lung tissue density was over 15%

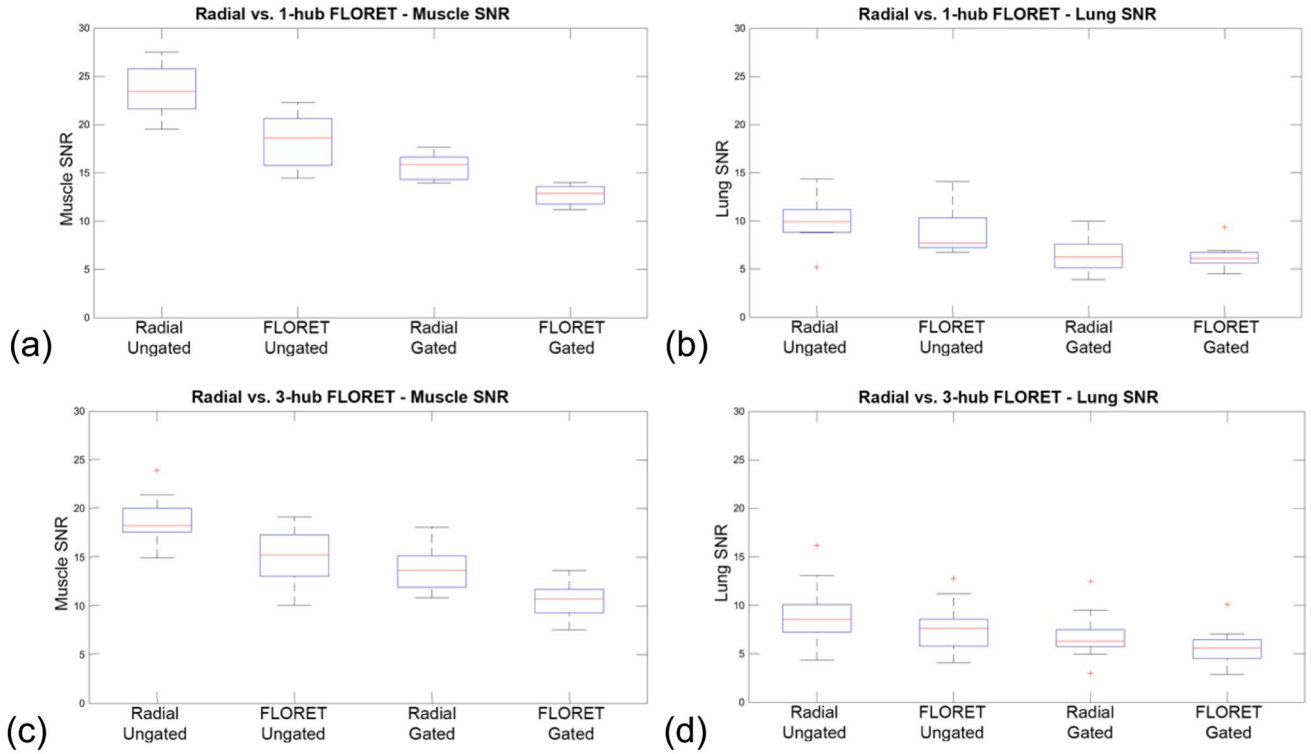

Fig. 6 Boxplots of SNR in radial vs. FLORET UTE in subjects scanned with 1-hub (**a**, **b**) and 3-hubs (**c**, **d**) from regions of muscle (**a**, **c**) and lung tissue (**b**, **d**), both with and without respiratory gating. Despite a factor of 4 reduction in scan time, SNR is only slightly lower in FLORET vs. radial UTE. Nonetheless, radial UTE has significantly higher SNR than its FLORET counterpart in all cases (except lung tissue with gating in 1-hub FLORET vs. radial UTE, panel b)

greater in 1-hub FLORET compared to estimates from radial UTE. The source of these discrepancies is not clear, particularly given no evidence of this phenomenon was present in phantom data. While speculative, it is possible that the noise measurement from a background ROI could be biased by the imaging trajectory given that potential artifacts (e.g., streaking, off-resonance or eddy currents) could manifest differently in each.

The influence of the off-resonance fat signal, in particular, could have a sequence-specific effect associated with the different point spread functions for fat and water within and between radial and FLORET trajectories. Additionally, this difference between radial and FLORET images manifests at the fat–water interfaces in the chest wall potentially impacting the normalized lung tissue density measurement and blurring contamination from fat signal, and eddy currents may artificially influence measurements of the standard deviation in the background leading to differences in normalized SNR between the two trajectories [34]. While beyond the scope of this work, mitigation of blurring due to fat by implementing either fat suppression [35] or multispectral fat–water separation techniques [36] is an important next step for improving performance. To further investigate effects of differences in the point spread function and their influences on effective resolution across sequences, we have performed experiments in a phantom with high-resolution features, detailed in the provided supplementary information.

A further potential source of bias is the theoretical values used to correct for differences in available transverse magnetization due to variations in flip angle and TR across sequences (Eqs. 2 and 3). In this work, we assume these efficiency comparisons are only modestly influenced by physiologic and disease-related relative regional proton density, T_1 and T_2*. This is a reasonable assumption for readout times that are short and comparable in duration which limit the impact of T_2* decay on the shape of the point spread function, and ensure signal is present for the duration of the total readout time. However, it is notable that we assume a lung and muscle T_1 derived from adult studies, which may not be consistent with values in the neonatal population. Deviations in the true T_1 will result in incorrectly normalized SNR; however, sensitivity analysis of the effects of true T_1 over the range of 900–1500 ms results in expected error of − 1.8 to 2.3% in the relative SNR normalization between radial and FLORET trajectories. Additionally, differences in the T_1 in lung vs. muscle would bias those tissues differently, causing an apparent difference in lung TD relative to muscle

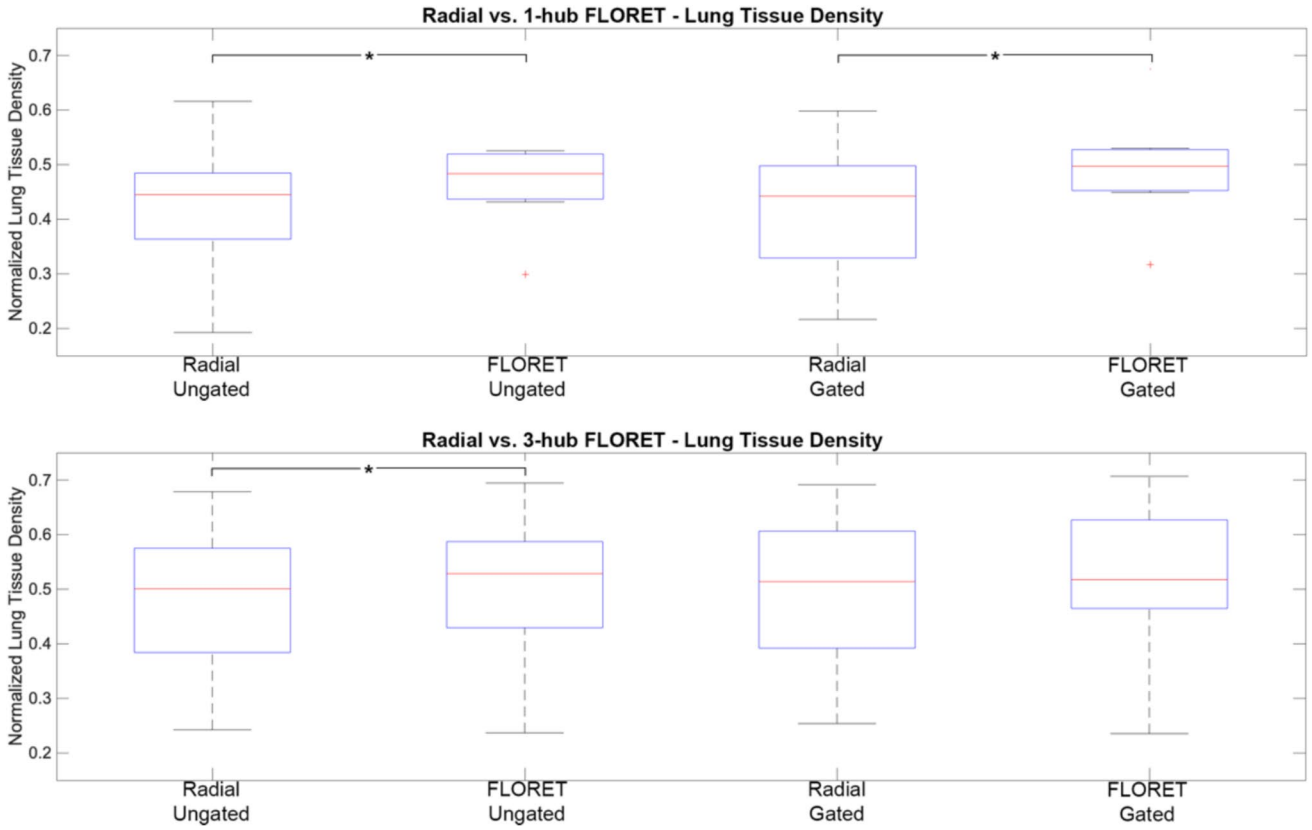

Fig. 7 Boxplots of normalized lung tissue density measurements in radial and FLORET UTE images from subjects scanned with 1-hub FLORET (**a**) and 3-hub FLORET (**b**), with and without respiratory gating. Lung tissue densities measured with FLORET are consistently higher than radial UTE ($P < 0.05$), although radial and 3-hub FLORET with respiratory gating do not achieve statistical significance. Statistically significantly different measurements are indicated by an asterisk. Normalized lung tissue density was estimated by dividing the lung signal by the adjacent muscle signal

Table 3 Radiologist reader scores on a Likert scale

Trajectory	Motion (1 low, 5 high)	Image quality (1 low, 5 high(	Pathology (1 low, 5 high)	Last visible airway generation
Radial	2.95 ± 1.00	2.71 ± 0.83	3.26 ± 0.74	2.19 ± 0.78
FLORET	2.67 ± 1.00	2.64 ± 0.96	3.31 ± 0.62	2.17 ± 0.76
P value of difference (population/pairwise)	0.35/0.29	0.80/0.62	0.82/0.72	0.92/0.88

with sequences that use different flip angles or TR. Future work is needed to quantify T1 of the lung parenchyma in the neonatal population.

Finally, B1+ heterogeneity is also a potential source of bias, both with respect to normalization of tissue densities and SNR. While the RF pulse and power (FA) are the same across trajectories, it is still possible that true FA may vary regionally. Given that TR was different between radial and FLORET UTE, this will have different effects in each. If B1+ in skeletal muscle varied significantly from lung parenchyma, the variable T1 weighting with each tissue type could bias the normalized tissue density across trajectories. Furthermore, the SNR normalization factor (Eqs. 2–5) depends on flip angle, and the relative normalization factors between radial and FLORET acquisitions will vary slightly with flip angle. While we expect B1+ variability to be less pronounced given the 1.5 T field strength, we cannot rule this out as a source of variability in our measurements.

This study has several important limitations. First, the phantom experiments were not performed with identical sequences on the same MRI scanner make and model as used for the in vivo studies. This was largely a practical issue because the NICU scanner used for in vivo imaging was decommissioned before phantom experiments could be

performed. However, the sequences (custom code designed in-house) were the same in both cases. The main goal of the phantom experiments was specifically to verify that radial and FLORET UTE yielded expected performance across a range of "tissue densities" (in this case, H_2O/D_2O concentrations) with short T_2* on the order of that expected for lung parenchyma, and it is unlikely that the differences in field strength should affect the relative performance of the two methods. However, it cannot be ruled out that deviations in performance between phantom and in vivo experiments are in part due to field-strength-related differences in the physics and experimental design. A second limitation of this study was the imperfect nature of the noise estimates for SNR calculation in vivo. Besides the aforementioned blurring due to fat/water chemical shift, using a background ROI for noise measurements potentially mixes deterministic and stochastic effects, and this has been shown to likely bias SNR comparisons of this nature [23]. Unfortunately, spending the time to acquire a separate noise scan was not feasible in this study population. Moreover, the maximum cone angle, $\alpha_{0,}$ was not optimized in this work and differed slightly between phantom and patient studies. While the values of α_0 were chosen here empirically as reasonable tradeoffs between improved $SNR_{efficiency}$ and orthogonal oversampling, we anticipate that different yet similar choices for α_0 will make a negligible difference. Additionally, given the nature of the neonatal imaging conditions, the potential influence of bulk motion cannot be ignored. Motion of this nature leads to increased blurring, but typically not to gross artifacts. However, the effect on SNR and normalized tissue density estimates could be variable and contribute to physiological noise. While we would not expect a bias toward a specific acquisition scheme, this is hard to validate. However, the differences in scan duration may influence the degree to which motion is present, and if present, the degree to which it influenced image quality. For example, a shorter scan may be less likely to be corrupted by episodic motion overall, but short durations of motion which sometimes occur in non-sedated neonates might affect a larger proportion of the scan. A precise evaluation of this effect requires a controlled experiment, which is not possible in this population and is beyond the scope of this experiment. Imaging was also performed using a single channel receive coil, which may not be representative of typical modern imaging platforms. The use of multi-channel receiver coils should not influence the SNR relationships between the two trajectories in theory. However, more practically, FLORET UTE could benefit from even further scan time reduction given that our current protocol oversamples (in the Nyquist sense) significantly. Thus, the number of views acquired could be further reduced without introducing aliasing or loss of effective resolution assuming the multiple receive channels can sufficiently improve the SNR in general. Finally, there is potential for systematic bias due to the non-randomized assignment of patients to either 1- or 3-hub FLORET. For example, changes in scanner performance or patient handling may change over time, affecting one cohort more or less than another.

To conclude, we have demonstrated the potential of FLORET UTE for neonatal pulmonary imaging in the NICU. These images are of quality comparable to radial UTE, the current state of the art, and have a much greater time-SNR efficiency which has enormous benefit in this sensitive population. Although we observed certain deviations in performance from theoretical predictions that require further attention, this technique paves the way for shorter exam times that are likely to make pulmonary UTE-based acquisitions more accessible and successful in neonatal patients.

Supplementary Information The online version contains supplementary material available at https://doi.org/10.1007/s10334-026-01368-1.

Author contributions Hahn—study conception and design, analysis and interpretation of data, drafting of manuscript. Willmering—study conception and design, acquisition of data, critical revision. Higano—study conception and design, acquisition of data, critical revision. Wharff—acquisition of data, critical revision. Fleck—acquisition of data, critical revision. Guillerman—acquisition of data, critical revision. Woods—study conception and design, critical revision. Fain—study conception and design, analysis and interpretation of data, critical revision.

Funding This study was funded by NIH/NHLBI R01 HL126771, R01 HL169765, R01 HL146689, R01 HL126774 and NIH/NCATS S10OD025025.

Data availability The data that support the findings of this study are not openly available due to reasons of sensitivity and are available from the corresponding author upon reasonable request. Data are located in controlled access data storage at the University of Iowa.

Declarations

Conflict of interest A.D. Hahn is a scientific advisor for Polarean LLC and receives consulting fees from Polarean LLC. M.M. Willmering is a scientific advisor for Polarean LLC and receives research support from Polarean LLC and Phillips Healthcare. N.S. Higano declares that she has no conflict of interest. C.J. Wharff declares he has no conflict of interest. R.J. Fleck declares he has no conflict of interest. R.P. Guillerman declares he has no conflict of interest. J.C. Woods declares he has no conflict of interest. S.B. Fain serves as a scientific advisor for Polarean LLC and receives research funding from Polarean LLC, Siemens Healthineers INC, GE Healthcare INC, and Sanofi/Regeneron INC for development of pulmonary CT and MRI methods.

Ethical approval Informed consent was obtained from the parents of the participants and patients in this study with ethical approval by the Cincinnati Children's Hospital and Medical Center investigational review board (IRB# 2018-0958).

References

1. Johnson KM et al (2013) Optimized 3D ultrashort echo time pulmonary MRI. Magn Reson Med 70(5):1241–1250
2. Hahn AD et al (2017) Pulmonary MRI of neonates in the intensive care unit using 3D ultrashort echo time and a small footprint MRI system. J Magn Reson Imaging 45(2):463–471
3. Adaikalam SA et al (2019) Neonatal lung growth in congenital diaphragmatic hernia: evaluation of lung density and mass by pulmonary MRI. Pediatr Res 86(5):635–640
4. Giltmier AJ et al (2023) Evaluation of regional lung mass and growth in neonates with bronchopulmonary dysplasia using ultrashort echo time magnetic resonance imaging. Pediatr Pulmonol. https://doi.org/10.1002/ppul.26705
5. Higano NS et al (2017) Quantification of neonatal lung parenchymal density via ultrashort echo time MRI with comparison to CT. J Magn Reson Imaging 46(4):992–1000
6. Yoder LM et al (2019) Elevated lung volumes in neonates with bronchopulmonary dysplasia measured via MRI. Pediatr Pulmonol 54(8):1311–1318
7. Adaikalam SA et al (2022) Tracheostomy prediction model in neonatal bronchopulmonary dysplasia via lung and airway MRI. Pediatr Pulmonol 57(4):1042–1050
8. Gunatilaka CC et al (2020) The effect of airway motion and breathing phase during imaging on CFD simulations of respiratory airflow. Comput Biol Med 127:104099
9. Bates AJ et al (2019) Quantitative assessment of regional dynamic airway collapse in neonates via retrospectively respiratory-gated (1) H ultrashort echo time MRI. J Magn Reson Imaging 49(3):659–667
10. Higano NS et al (2018) Neonatal pulmonary magnetic resonance imaging of bronchopulmonary dysplasia predicts short-term clinical outcomes. Am J Respir Crit Care Med 198(10):1302–1311
11. Gouwens KR et al (2020) Magentic resonance imaging evaluation of regional lung Vts in severe neonatal bronchopulmonary dysplasia. Am J Respir Crit Care Med 202(7):1024–1031
12. Higano NS et al (2022) Virtual bronchoscopy of neonatal airway malacia via high-resolution, respiratory-gated magnetic resonance imaging. Am J Respir Crit Care Med 206(5):e42–e43
13. Gunatilaka CC et al (2022) Predicting tracheal work of breathing in neonates based on radiological and pulmonary measurements. J Appl Physiol 133(4):893–901
14. Hysinger EB et al (2020) Ultrashort echo-time MRI for the assessment of tracheomalacia in neonates. Chest 157(3):595–602
15. Gunatilaka CC et al (2021) Neonates with tracheomalacia generate auto-positive end-expiratory pressure via glottis closure. Chest 160(6):2168–2177
16. Hahn AD et al (2020) Characterization of R2 * and tissue density in the human lung: application to neonatal imaging in the intensive care unit. Magn Reson Med 84(2):920–927
17. Hahn AD et al (2021) Effects of neonatal lung abnormalities on parenchymal R(2) * estimates. J Magn Reson Imaging 53(6):1853–1861
18. Higano NS et al (2017) Retrospective respiratory self-gating and removal of bulk motion in pulmonary UTE MRI of neonates and adults. Magn Reson Med 77(3):1284–1295
19. Pipe JG et al (2011) A new design and rationale for 3D orthogonally oversampled k-space trajectories. Magn Reson Med 66(5):1303–1311
20. Stobbe RW, Beaulieu C (2021) Three-dimensional Yarnball k-space acquisition for accelerated MRI. Magn Reson Med 85(4):1840–1854
21. Willmering MM et al (2019) Implementation of the FLORET UTE sequence for lung imaging. Magn Reson Med 82(3):1091–1100
22. Meadus WQ et al (2021) Quantification of lung water density with UTE Yarnball MRI. Magn Reson Med 86(3):1330–1344
23. Robison RK, Anderson AG 3rd, Pipe JG (2017) Three-dimensional ultrashort echo-time imaging using a FLORET trajectory. Magn Reson Med 78(3):1038–1049
24. Duyn JH et al (1998) Simple correction method for k-space trajectory deviations in MRI. J Magn Reson 132(1):150–153
25. Jackson JI et al (1991) Selection of a convolution function for Fourier inversion using gridding [computerised tomography application]. IEEE Trans Med Imaging 10(3):473–478
26. Pipe JG, Menon P (1999) Sampling density compensation in MRI: rationale and an iterative numerical solution. Magn Reson Med 41(1):179–186
27. Schindelin J et al (2012) Fiji: an open-source platform for biological-image analysis. Nat Methods 9(7):676–682
28. Wang D et al (2023) High SNR rapid T(1) -weighted MPRAGE using spiral imaging with long readouts and improved deblurring. Magn Reson Med 89(3):951–963
29. Nofiele JT, Cheng HL (2013) Ultrashort echo time for improved positive-contrast manganese-enhanced MRI of cancer. PLoS ONE 8(3):e58617
30. Tkach JA et al (2014) MRI in the neonatal ICU: initial experience using a small-footprint 1.5-T system. AJR Am J Roentgenol 202(1):W95–W105
31. Pratt R et al (2015) A novel switched frequency 3He/1H high-pass birdcage coil for imaging at 1.5 tesla. Concepts Magn Reson Part B Magn Reson Eng 45(4):174–182
32. Mathur AM et al (2008) Transport, monitoring, and successful brain MR imaging in unsedated neonates. Pediatr Radiol 38(3):260–264
33. Dietrich O, Gaass T, Reiser MF (2017) T1 relaxation time constants, influence of oxygen, and the oxygen transfer function of the human lung at 1.5T-A meta-analysis. Eur J Radiol 86:252–260
34. Willmering MM et al (2025) High-quality FLORET UTE imaging for clinical translation. Magn Reson Med 93(1):276–288
35. de Kerviler E et al (1998) Fat suppression techniques in MRI: an update. Biomed Pharmacother 52(2):69–75
36. Reeder SB et al (2007) Water-fat separation with IDEAL gradient-echo imaging. J Magn Reson Imaging 25(3):644–652